V European Conference on Computational Fluid Dynamics
ECCOMAS CFD 2010
J. C. F. Pereira and A. Sequeira (Eds)
Lisbon, Portugal,14-17 June 2010

DELAYED DETACHED EDDY SIMULATION OF AERODYNAMIC CONTROL WITH SYNTHETIC JETS

Sol Keun Jee*, Omar López†, Daniel Brzozowski‡, Ari Glezer‡, Robert Moser⋆

*Department of Mechanical Engineering, University of Texas at Austin
Austin, Texas, USA
e-mail: solkeun@ices.utexas.edu
†Departamento de ingenieria mecánica, Universidad de los Andes
Bogota, Colombia
e-mail: od.lopez20@uniandes.edu.co
‡Woodruff School of Mechanical Engineering, Georgia Institute of Technology
Atlanta, Georgia, USA
e-mail: {danb, ari.glezer}@gatech.edu
⋆Department of Mechanical Engineering, Institute for Computational Engineering and Sciences
Austin, Texas, USA
e-mail: rmoser@ices.utexas.edu

Key words: Synthetic Jet, Flow Control, Detached Eddy Simulation

Abstract. *There has been an increasing interest in using synthetic jets to control small scale unmanned aerial vehicles (UAVs) due to their faster response and lighter structure than conventional control surfaces. In this research, aerodynamic control with synthetic jets is investigated using CFD with delayed detached eddy simulation [1] based on the Spalart-Allmaras (SA) one-equation eddy viscosity model [2]. Following the wind-tunnel experiments conducted by Brzozowski et. al. [3], two synthetic jet actuators are mounted on a NACA 4415 airfoil to bi-directionally change the aerodynamic forces. The numerical simulation is conducted at a Reynolds number* $Re = 9 \times 10^5$*, with Strouhal number of the synthetic jet* $St_{sj} = 32$ *and small angles of attack in the range of 0 to 6 deg. The modified airfoil generates complicated vortical strucutures because separating shear layers become unstable, roll up to form vortices and interact with recirculating flow downstream. The synthetic jet actuation provides additional momentum transfer in the wall-normal direction, which leads to the deflection of the streamlines close to the airfoil surface and changes the pressure distribution along the airfoil surface, all of which create bi-directional changes in the aerodynamic forces. The current computation is compared with wind-tunnel experiments, and the difference between the two is discussed.*

1 Introduction

A synthetic jet (also called zero-net-mass-flux jet) is typically "synthesized" by periodically alternating ejection and suction of fluid through an orifice, which is produced by oscillating pressure commonly generated by the motion of a diaphragm [4, 5] or a piston [6] or acoustic waves [7] in a cavity (see Figure 1). While the flow during the suction phase is similar to a sink flow, the flow during the ejection separates at the sharp edge of the orifice and produces vortices (vortex rings or vortex pairs for circular or two-dimensional jets, respectively) which entrain the surrounding fluid and move away from the orifice with their self-induced velocity. This jet has zero-net mass flux but non-zero momentum flux due to the asymmetry between suction and ejection. Consequently, synthetic jets can transfer momentum to the surrounding working fluid without injecting net mass. This unique feature makes them attractive fluid actuators in numerous flow control applications, especially controlling aerodynamic performance.

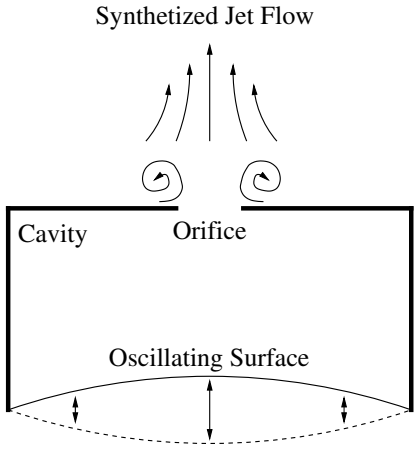

Figure 1: Schematic diagram of a synthetic jet actuator

DeSalvo *et. al.* [4] reported bi-directional changes in the pitching moment using two synthetic jet actuators on the top and bottom of an airfoil near the trailing edge, without moving control surfaces. The synthetic jets control the wake vorticity, which manipulates the Kutta condition of the airfoil. Brzozowski *et. al.* [5, 3] and Muse *et. al.* [8] explored the bi-directional changes to demonstrate rapid maneuvering airfoils with a closed-loop control system. Our previous computational research represented this unique feature [9, 10] and studied the bi-directional changes coupled with motions of the airfoil including the closed-loop control system [11].

In this research, we investigate the airfoil used by Brzozowski *et. al.* [3]. Compared with the airfoil studied in earlier computational and experimental studies including [5, 9, 11], the current airfoil generates significant flow separation because of the upstream location of the suction side actuator. Therefore, it is imperative to examine the effects of

the synthetic jet on this significant separation region.

The numerical methods used in the current study are summarized and validated in Section 2 which also includes the details of the current airfoil and the synthetic jet actuators. The effects of the synthetic jet on the flow field are discussed in Section 3. The current computational results are compared with experimental results in the case of an unmodified airfoil in Section 2.4 and in the case of the modified airfoil in Section 3.

2 Numerical Methods

The Spalart-Allmaras (SA) model and detached eddy simulation (DES) have been developed for engineering aerodynamic flows at high Reynolds number. Although DES could be based on various eddy viscosity models including $k-\epsilon$ and $k-\omega$ models and Reynolds stress transport models, we use extended delayed DES (EDDES) [1] based on a SA model. Among several versions of the SA model, we use the standard version with $f_{\nu 3}$ term proposed by Desk *et. al.* [2]. The EDDES-SA model is summarized for the completeness.

2.1 Spalart-Allmaras model

The SA equation is a convection-diffusion equation with source terms to control the generation and destruction of the model variable $\tilde{\nu}$

$$\frac{\partial \tilde{\nu}}{\partial t} + u_j \frac{\partial \tilde{\nu}}{\partial x_j} = \underbrace{c_{b1}\tilde{S}\tilde{\nu}}_{\text{production}} \underbrace{- c_{w1} f_w \left(\frac{\tilde{\nu}}{d}\right)^2}_{\text{destruction}} + \underbrace{\frac{1}{\sigma}\left[\frac{\partial}{\partial x_j}\left((\nu+\tilde{\nu})\frac{\partial \nu}{\partial x_j}\right) + c_{b2}\frac{\partial^2 \tilde{\nu}}{\partial {x_i}^2}\right]}_{\text{diffusion}}. \quad (1)$$

The turbulence eddy viscosity ν_t is computed from $\nu_t = \tilde{\nu} f_{\nu 1}$ and $f_{\nu 1}$ is given by

$$f_{\nu 1} = \frac{\chi^3}{\chi^3 + {c_{\nu 1}}^3}, \quad (2)$$

$$\chi = \frac{\tilde{\nu}}{\nu}. \quad (3)$$

The SA model admits the log law as a solution (*i.e.* $\tilde{\nu} = \kappa y u_\tau$ in the log layer), and the damping function $f_{\nu 1}$ is formulated for the buffer layer and viscous sublayer. $\tilde{S}$ in the production term in Equation 1 is written by

$$\tilde{S} = \tilde{f}_{\nu 3} S + \frac{\tilde{\nu}}{\kappa^2 d^2}\tilde{f}_{\nu 2}, \quad (4)$$

where d is the distance from the wall, κ is the von Karman constant, and the function $\tilde{f}_{\nu 2}$ and $\tilde{f}_{\nu 3}$ are given by

$$\tilde{f}_{\nu 2} = \left(1 + \frac{\chi}{c_{\nu 2}}\right)^{-3} \quad (5)$$

$$\tilde{f}_{\nu 3} = \frac{(1+\chi f_{\nu 1})(1-\tilde{f}_{\nu 2})}{\chi}. \quad (6)$$

The parameter S is commonly the magnitude of vorticity, *i.e.,* $S = \sqrt{2\Omega_{ij}\Omega_{ij}}$ where the rotation tensor $\Omega_{ij} = 1/2\,(\partial U_i/\partial x_j - \partial U_j/\partial x_i)$. Equation 4-6 with the constant $c_{\nu 2} = 5$ are suggested by Deck *et. al.* [2] to prevent negative values of the production term in the SA equation.

In the destruction term of the SA equation (Equation 1), f_w is given by:

$$f_w = g\left[\frac{1 + {c^6}_{w3}}{g^6 + {c^6}_{w3}}\right]^{1/6}, \tag{7}$$

where g is defined as

$$g = r + c_{w2}\left(r^6 - r\right), \tag{8}$$

$$r = \min\left(\frac{\tilde{\nu}}{\tilde{S}\kappa^2 d^2}, 10\right). \tag{9}$$

The dependent parameter r of the function f_w indicates pressure gradient close to the wall: adverse and favorable pressure gradient for $r > 1$ and $r < 1$, respectively. The function $f_w(r)$ guarantees a fast decaying behavior of destruction in the outer region of the boundary layer.

Finally, the constants that appear in Eq. 1-9 are defined by following Spalart *et. al.* [12]: $\sigma = 2/3$, $c_{b1} = 0.1355$, $c_{b2} = 0.622$, $\kappa = 0.41$, $c_{w2} = 0.3$, $c_{w3} = 2$, $c_{\nu 1} = 7.1$, $c_{w1} = \frac{c_{b1}}{\kappa^2} + \frac{1+c_{b2}}{\sigma}$. The first three coefficients are calibrated for correct levels of shear stress in 2D mixing layers and wakes. The coefficients c_{w2}, c_{w3} and $c_{\nu 1}$ are determined from a flat-plate boundary layer with zero pressure gradient. The last coefficient c_{w1} is derived to obtain the equilibrium between the sum of production and diffusion term and the destruction term in the log layer.

2.2 EDDES Turbulence Model

DES is a 3D unsteady numerical solution using a single turbulence model, which functions as a sub-grid-scale model in regions where grid density is fine enough for LES (*e.g.,* separated flows), and as a RANS in regions where it is not (*e.g.,* attached boundary layers). The destruction term in Equation 1 is proportional to $(\nu/d)^2$. When balanced with the production term, the destruction term adjusts the eddy viscosity to scale with the local deformation rate S and the wall distance d, *i.e.,* $\tilde{\nu} \propto Sd^2$. The Smagorinsky model scales its Sub-Grid-Scale (SGS) eddy viscosity with S and grid spacing Δ: $\nu_{SGS} \propto S\Delta^2$. Thus Spalart *et. al.* [13] suggested that the SA model with d replaced by $\tilde{d}$ defined by

$$\tilde{d} = \min(d, C_{DES}\Delta), \tag{10}$$

can be a SGS model when $\Delta \ll d$. The constant $C_{DES} = 0.65$ is calibrated for homogeneous turbulence. This is the first version of DES (commonly referred as DES97). Two common definitions for the sub-grid filter Δ are $\Delta = \max(\Delta x, \Delta y, \Delta z)$ for structured

grids and Δ = (cell volume)$^{1/3}$ for unstructured grids. Spalart *et. al.* [14] improves the formulation of $\tilde{d}$ to avoid "grid-induced separation" in DES97 by using the following formula instead:

$$\tilde{d} = d - f_d \max(0, d - C_{DES}\Delta), \tag{11}$$

where the function f_d is given by

$$f_d = 1 - tanh([8r_d]^3), \tag{12}$$

which is steep near $r_d = 0.1$ and indicates LES and RANS regions when $f_d \simeq 1$ and $f_d \simeq 0$, respectively. The parameter r_d in Eq. 12 is written as

$$r_d = \frac{\nu_t + \nu}{\sqrt{U_{i,j}U_{i,j}}\kappa^2 d^2}, \tag{13}$$

where $U_{i,j} = \frac{\partial U_i}{\partial x_j}$.

An extension of DDES (EDDES) was proposed by Riou *et. al.* [1] to achieve fast transaction from RANS to LES outside of boundary layers. The main idea of EDDES is to enforce the functions $f_{\nu 1}$, $\tilde{f}_{\nu 2}$ and f_w used in the SA model (Section 2.1) to have their asymptotic values depending on RANS or LES region. Riou *et. al.* [1] also suggested to use different definition of the sub-grid filter Δ depending on RANS or LES region because structured and unstructured grids are commonly used in boundary layers (RANS) and wakes (LES), respectively. EDDES accelerates the destruction of the eddy viscosity in LES regions, which ensures a fast development of instabilities. The modifications of DDES used in EDDES are summarized as follows:

$$\text{If } f_d < f_{do}, \quad \text{then } \Delta = \max(\Delta x, \Delta y, \Delta z),\ \text{unchanged} f_{\nu 1},\ f_{\nu 2},\ f_w \tag{14}$$

$$\text{If } f_d \geq f_{do}, \quad \text{then } \Delta = (\text{cell volume})^{1/3},\ f_{\nu 1} = f_w = 1,\ f_{\nu 2} = 0 \tag{15}$$

where the cut-off value $f_{do} = 0.8$ in general.

2.3 Incompressible Navier-Stokes Solver

The EDDES-SA turbulence model is implemented in an incompressible Navier-Stokes solver CDP [15] developed at the Center for Turbulence Research (CTR) at Stanford University. The solver is based on finite-volume spatial discretization with second-order accuracy, and a second-order fully implicit fractional step method. CDP employs a novel collocated formulation to conserve mass, momentum and kinetic energy (in the inviscid limit) in a hybrid unstructured mesh. The details of the implementation of the turbulence model in CDP are documented in [9].

2.4 Validation of EDDES Turbulence Model

To validate the EDDES-SA turbulence model (Section 2.1 and 2.2), we simulate the flow field over a NACA 4415 airfoil at $Re = 9 \times 10^5$ and small angles of attack over the

range $-2^o \leq \alpha \leq 10^o$. This is the basic case for the primary flow control study in Section 3. Figure 2 shows the current CFD results match the legacy data [16] and the more recent experiments of Hoffmann *et. al.* [17]. There is, however, a discrepancy between our wind-tunnel data and the others in Figure 2. The discrepancy is perhaps caused by the open slot in the wind-tunnel side walls (shown in Figure 2(c)) needed to accommodate the traverse for experiments on maneuvering airfoils [8, 5]. The slots could cause a net reduction of suction (increased pressure) on the airfoil (Figure 2(b)) resulting a lower lift (Figure 2(a)). This discrepancy between the current CFD and experiments on the NACA 4415 airfoil suggests that similar discrepancy should be expected for the modified airfoil in Section 3. The wind-tunnel walls are not included in the current simulation because (1) computing the walls is numerically expansive and (2) our ultimate interest is the performance of synthetic jets in a free-flight airfoil (not discussed in this report).

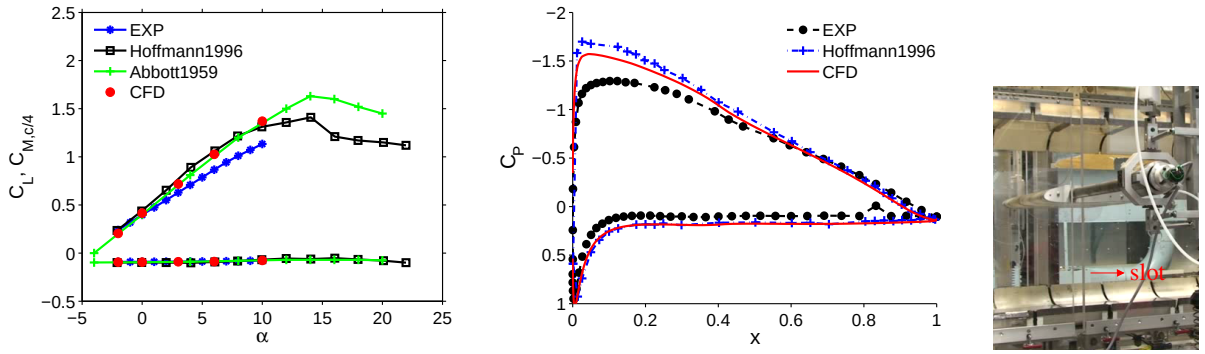

(a) $C_L, C_{M,c/4}$ (b) C_p at $\alpha = 6^o$ (c) open slot

Figure 2: The current simulation and experimental results of the NACA 4415 airfoil at $Re \simeq 10^6$. The legacy data of Abbott *et. al.* [16] and the separate experimental wind-tunnel data of Hoffmann *et. al.* [17] are used to validate the current results. The difference between the current experiment and others is perhaps caused by the open slots which are required for experiments on maneuvering airfoils [8, 5]. The wind-tunnel walls are not included in the computation.

2.5 Simulation Setup

Figure 3 shows the modified NACA 4415 airfoil which includes two synthetic jet actuators near the trailing edge. The location of the actuators was determined to maximize the effects of the synthetic jet via the experimental study [3]. The round surface between the actuator outlet and the base NACA 4415 airfoil is designed to take advantage of the the Coanda effect.

The cavity of the actuator used in the current simulation is smaller than the real one because there was no significant two-way coupling between the external flow and the flow in the cavity in previous simulations [9]. Since the interaction of the jet with the

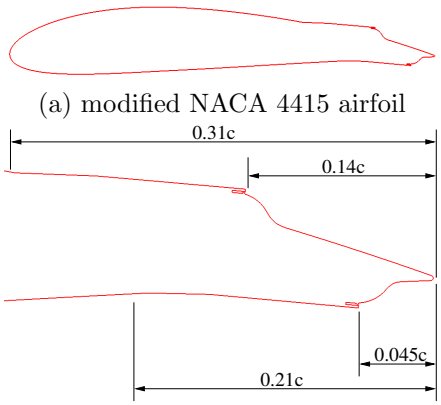

(a) modified NACA 4415 airfoil

(b) details of the modification

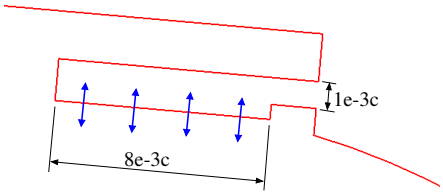

(c) oscillating velocity boundary condition

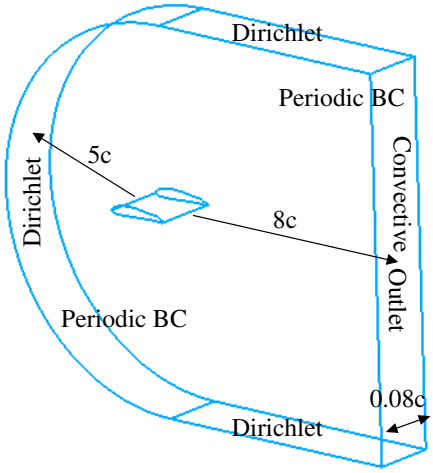

(d) computation domain

Figure 3: The current modified NACA 4415 airfoil and computation domain

surrounding characterizes the synthetic jet, the small portion of the real cavity is included in the computation. The oscillating normal velocity boundary condition

$$U_n = |U_n| \sin(2\pi\ St_{sj}\ t) \tag{16}$$

is applied at the bottom surface of the cavity to simulate the oscillation of the piezoelectric diaphragm shown in Figure 4. The amplitude of the boundary condition $|U_n| = 0.18u_\infty$ is determined by the momentum coefficient of the synthetic jet $C_\mu = {u^2}_{sj,rms} A_{sj}/(1/2\rho {u^2}_\infty A) = 2.2 \times 10^{-3}$ with Strouhal number $St_{sj} = f_{sj}c/u_\infty = 32$, following the current experiments. The rms (root-mean-square) velocity of the synthetic jet at the actuator outlet $u_{sj,rms}$ is obtained from the computational results in Section 3. The ratio of the jet outlet area A_{sj} to the planform area A is $A_{sj}/A = 0.001$. A convective time scale $t_c = c/u_\infty$ is used to obtain a dimensionless time variable $t = \tilde{t}/t_c$ where $\tilde{t}$ is a dimensional variable.

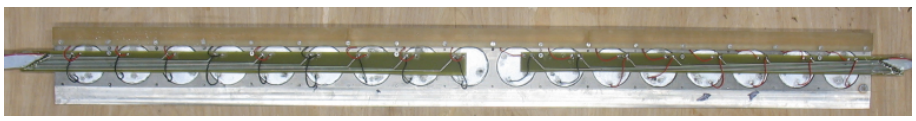

Figure 4: The bottom view of the actuator used in the experiment shows an array of 17 disks which are the oscillating piezoelectric diaphragm.

The size of the computation domain and the boundary conditions are shown in Figure 3(d). The domain is periodic in the spanwise direction, and the spanwise dimension is equivalent to the size of a single actuator module uniformly distributed in the 1×17 array actuator used in the experiment (shown in Figure 4). The first grid size in the wall normal direction on the airfoil is $\Delta_y \lesssim y^+$, and the grid size in the LES part of the DES near the airfoil is $\Delta_{x,y,z} \lesssim 0.005c$. The value of the model variable $\tilde{\nu}$ of the SA equation (Equation 1) is $\tilde{\nu} = 0.1\nu$ at the outer boundary, and computation results are not sensitive to this value if $\tilde{\nu} \lesssim \nu$. The numerical simulation and experiments are conducted at a Reynolds number $Re = 9 \times 10^5$. The experimental setup is documented in [5].

3 Results

The current modified NACA 4415 airfoil generates interesting flow phenomena which were not observed around either the clean airfoil or the former modified airfoil (see Figure 5). While the boundary layers are fully attached on the clean airfoil, they separates at the sharp edge of the actuators of the two modified airfoils. While the former modified airfoil generates well-organized shedding vortices because of the symmetric location of the top and bottom actuator near the trailing edge, the current modified airfoil generates complicated vortical structures. The flow field around the current airfoil will be analyzed in this report, and the detailed results of the former modified airfoil are included in previous studies [5, 9, 11].

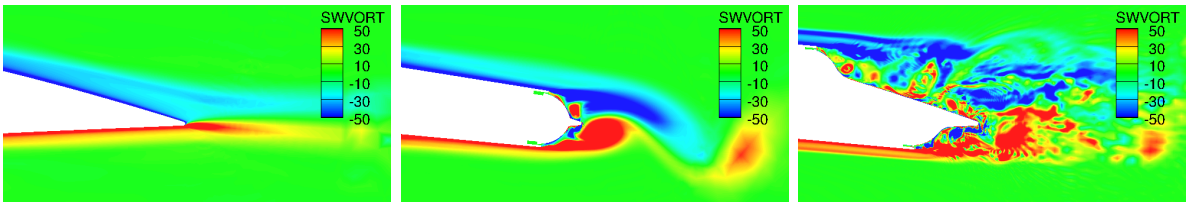

(a) NACA 4415 airfoil (b) former modified NACA 4415 airfoil without actuation (c) current modified NACA 4415 airfoil without actuation

Figure 5: Instantaneous spanwise vorticity field of the clean, former modified and current modified airfoil at $\alpha = 3^o$. The detailed results of the former modified airfoil are documented in previous studies [5, 9, 11]

For the current modified airfoil, the boundary layer separates at the sharp edge of the actuator, becomes an unstable shear layer, rolls up to form vortices and interacts with the recirculating flow downstream of the actuator, all of which are associated with the complicated vortical structures. Since the suction side (SS or top) actuator is located far enough upstream of the trailing edge, the recirculation region is large similar to a typical backward-facing-step flow. The aerodynamic lift of this airfoil is less than that of the clean airfoil (see Figures 2(a) and 6) due to the flow separation. Figure 6 shows that the current results are within the uncertainty of the current experimental data, and the slope

of the lift is higher in CFD, which is consistent with the difference between the CFD and the experimental data of the clean airfoil as shown in Figure 2.

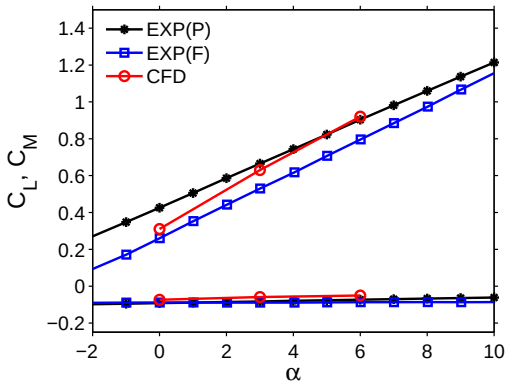

Figure 6: Aerodynamic lift and moment of the modified NACA 4415 airfoil without actuation. The experimental results are obtained from pressure (P) and direct force (F) measurement.

When the synthetic jet actuators are active, the turbulence in the separation region near the actuator is enhanced (see Figure 7), which increases mixing and reduces the size of the separation region (see Figure 8). Both the suction side (SS) and pressure side (PS) actuation pull the averaged vorticity field close to the airfoil surface. Compared with the experimental data, the simulation overestimates the size of the recirculation region on the top in the absence of the actuation (Figure 8(c)), which leads to the narrow recirculation region in the SS actuation (Figure 8(a)) which is not observed in the corresponding PIV data (Figure 8(b)).

The synthetic jet changes the overall pressure distribution on the airfoil and more dramatically near the actuator as shown in Figure 9. Pressure drops around the actuator because the synthetic jet injects additional momentum and kinetic energy into the surrounding fluid. PS actuation generates a downward force at the tail, producing a pitch-up moment. It is exactly opposite to SS actuation. This bi-directional change of aerodynamic forces has been observed in similar airfoils with two tangential synthetic jet actuators in our previous experiments [5, 3] and computations [9, 11]. The current computation overestimates pressure around the upstream intersection of the SS actuator and the base NACA 4415 airfoil because the CFD airfoil has a sharp intersection while the wind-tunnel model is rounded with a aluminum tape as shown in Figure 9(c).

The time-dependent aerodynamic lift and moment with and without actuation are shown in Figure 10. Without actuation, the aerodynamic lift and moment oscillate because of the vortex shedding off the actuators. The oscillation (without actuation) is not as regularly periodic as was observed in previous studies [5, 9, 11], in which the former modified airfoil was used. The synthetic jet imposes more rapid oscillation ($St_{sj} = 32$),

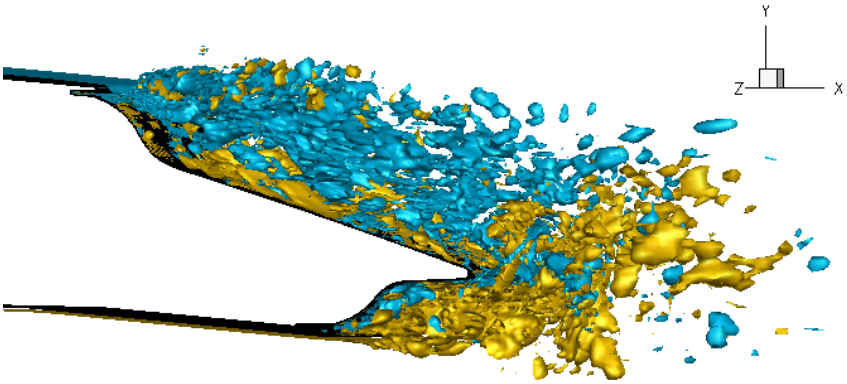

(a) suction side (SS or top) actuation

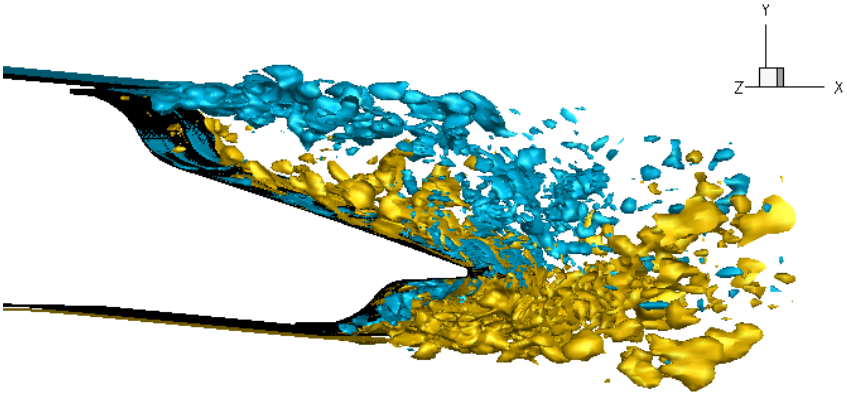

(b) no actuation

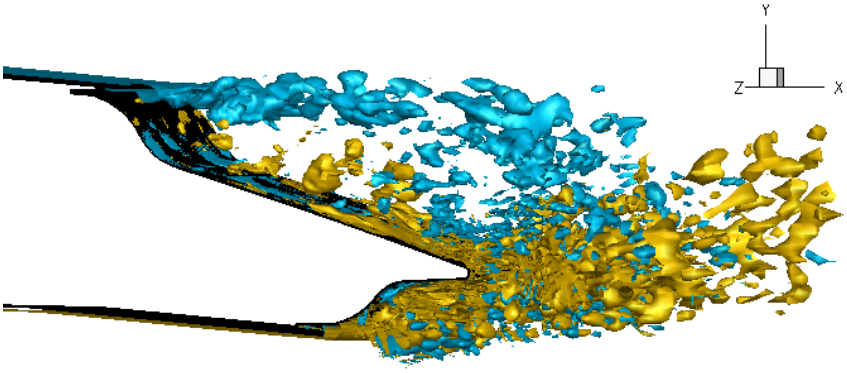

(c) pressure (PS or bottom) actuation

Figure 7: Instantaneous spanwise vorticity $\omega_z \pm 70$ with and without actuation at $\alpha = 3^o$

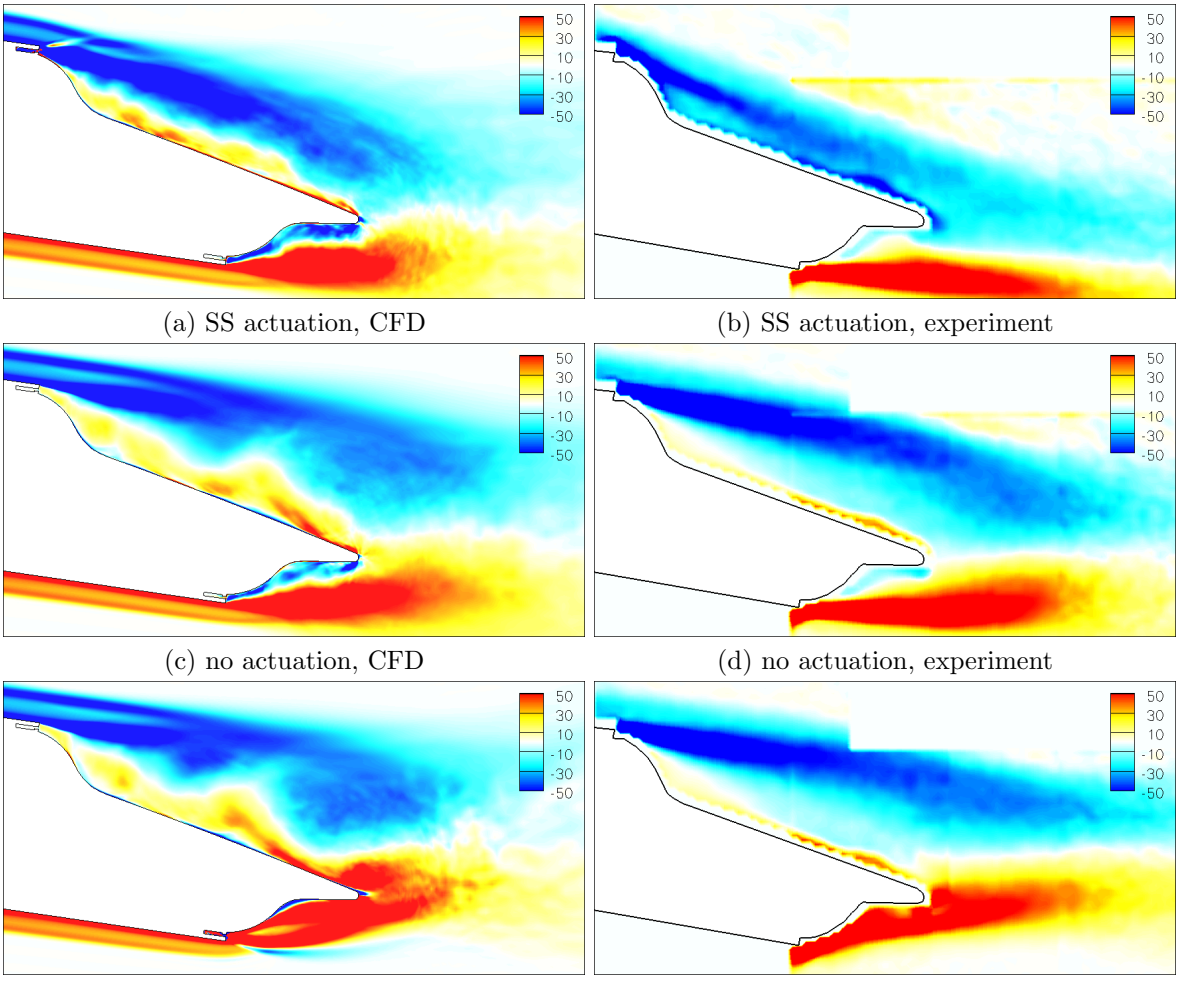

(a) SS actuation, CFD

(b) SS actuation, experiment

(c) no actuation, CFD

(d) no actuation, experiment

(e) PS actuation, CFD

(f) PS actuation, experiment

Figure 8: Time-averaged spanwise vorticity fields with and without actuation in CFD and experimental data at $\alpha = 3^o$

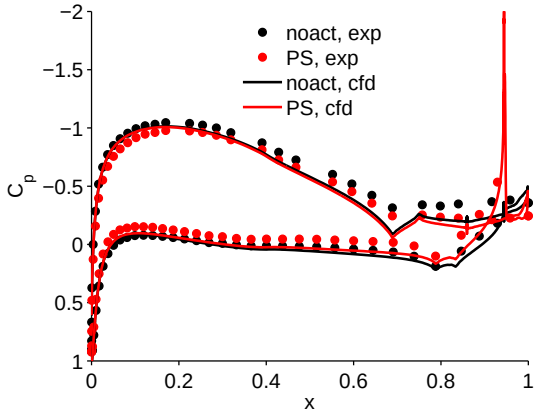

(a) C_p without actuation and with PS actuation

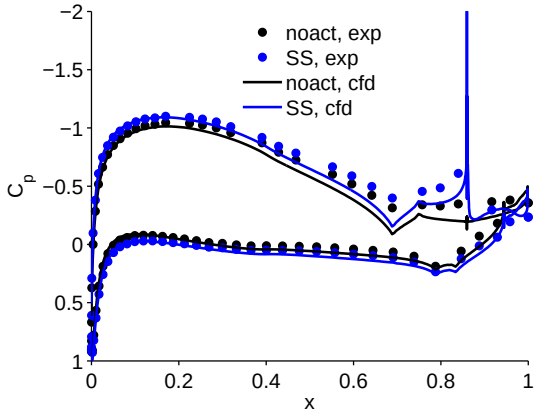

(b) C_p without actuation and with SS actuation

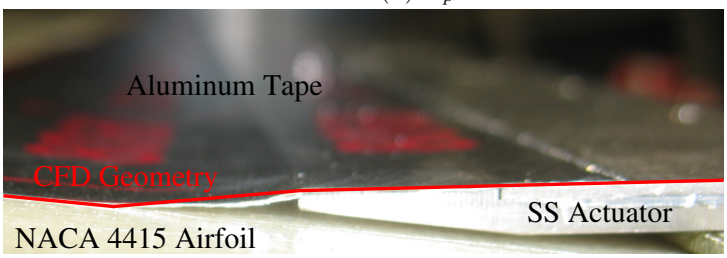

(c) CFD and experiment geometry around the upstream SS actuator

Figure 9: Pressure distribution of the modified NACA 4415 airfoil with and without actuation at $\alpha = 3^o$. The sharp corner at the upstream SS actuator of the CFD geometry causes higher pressure at the corner than the experiment.

and bi-directionally shifts the aerodynamic forces within one convective time scale t_c. The changes in the aerodynamic forces are summarized in Figure 11. The simulation results qualitatively match the experimental data. The major difference is that the effects of the SS actuation depend on the angle of attack in the current CFD but not in the experiment. The angle dependence was also observed in previous experimental [5] and computational studies [9, 11] of the former airfoil.

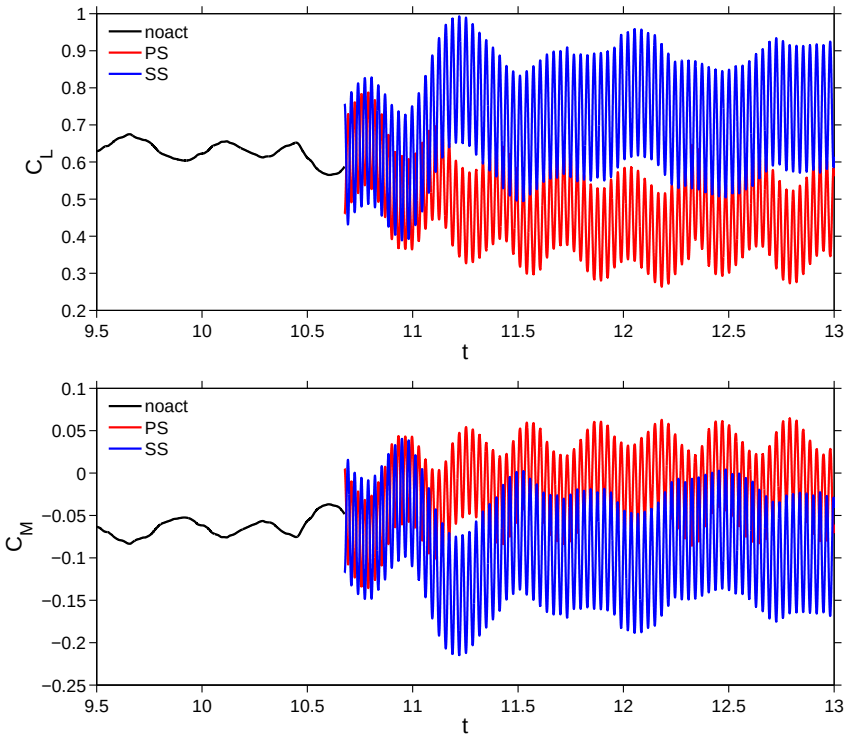

Figure 10: Aerodynamic lift and moment with and without actuation at $\alpha = 3^o$. A convective time scale $t_c = c/u_\infty$ is used for the dimensionless time variable $t = \tilde{t}/t_c$ where $\tilde{t}$ is a dimensional time variable.

The mean and rms (root-mean-square) of the normal and tangential velocity at the actuator outlet are asymmetric about the center of the outlet because the surrounding environment of the outlet is asymmetric as well (see Figure 12). For this reason, a small portion of the cavity is kept in the simulation that the synthetic jet is modeled properly. Without the cavity, for example, a common boundary condition at the outlet (oscillating normal velocity u_n and zero-gradient of tangential velocity u_t) would oversimplify the interaction between the flow at the outlet and the surroundings, and could misrepresent the asymmetric velocity profiles.

The synthetic jet actuation removes the secondary circulation flow observed in the case of no actuation (Figure 12(d) and (h)), because the significant pressure drop at

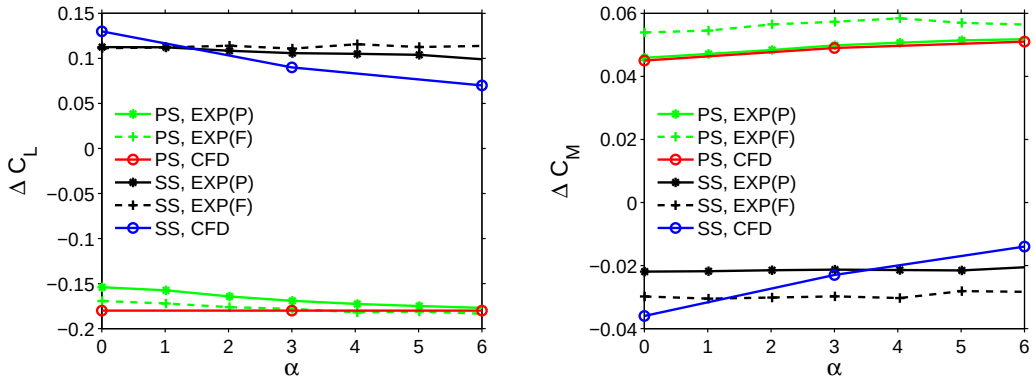

Figure 11: Change of aerodynamic lift and moment due to actuation. The experimental results are obtained through pressure (P) and direct force (F) measurement.

the outlet draws the flow along the Coanda surface, leaving only the main recirculation near the outlet during the actuation. Figure 12 (c) and (d) (or (g) and (h)) shows that the streamline at the sharp edge of the actuator deflects toward the airfoil surface after the actuation. The rms velocity $u_{sj,rms} = \sqrt{u^2{}_{n,rms} + u^2{}_{t,rms}}$ is used to compute the synthetic jet momentum coefficient $C_\mu = 2.2 \times 10^{-3}$ which agrees with the experimental C_μ measured with a hot-wire anemometer.

4 Conclusions

The current modified NACA 4415 airfoil generates interesting flow phenomena which were not observed around either the clean airfoil or the former modified airfoil. The boundary layer separates at the sharp edge of the actuator, becomes an unstable shear layer, rolls up to form vortices and interacts with the recirculating flow downstream, all of which are associated with complicated vortical structures in the wake. The significant flow separation on the suction side of the airfoil causes a large recirculation region and less aerodynamic lift compared with the clean NACA 4415 airfoil.

The top and bottom synthetic jet actuation generates more vortices in each recirculation region, which results in more momentum transfer in the wall normal direction due to mixing. Consequently, the streamlines are deflected toward the airfoil surface, and the pressure distribution along the airfoil is changed. The significant local drop of pressure near the actuation causes the bi-directional changes in aerodynamic forces. The asymmetric profiles of the synthetic jet velocity at the actuator outlet indicate the necessity of the cavity in the computational study to include the flow interaction between the jet and the surrounding flow.

The EDDES-SA turbulence model represents the aerodynamics and the instability in the separating shear layer. The current computation has qualitatively good agreement with the experiment on the effects of synthetic jets on the flow field. Unavoidable differ-

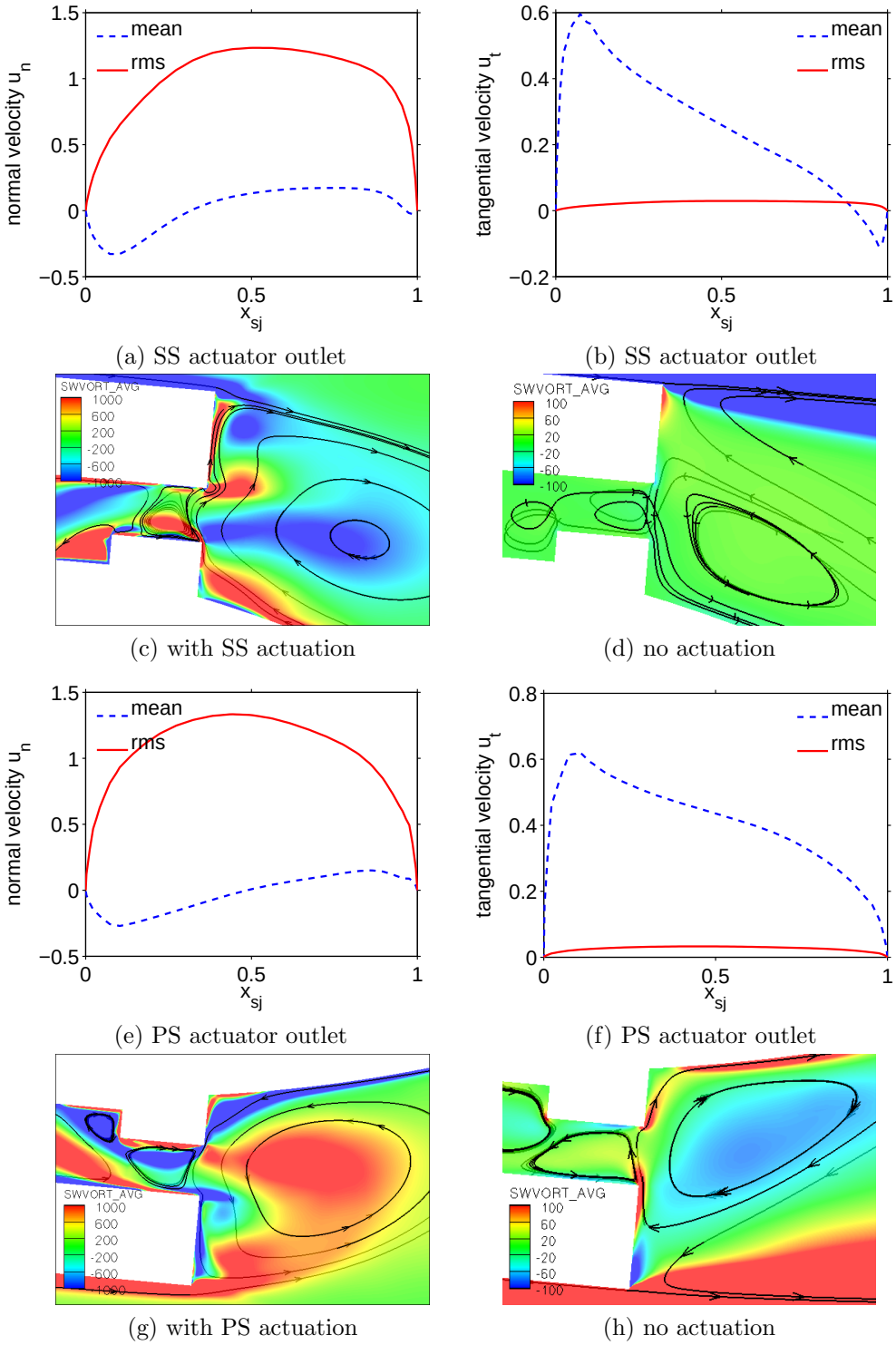

(a) SS actuator outlet

(b) SS actuator outlet

(c) with SS actuation

(d) no actuation

(e) PS actuator outlet

(f) PS actuator outlet

(g) with PS actuation

(h) no actuation

Figure 12: Statistics of velocity (normalized by the freestream velocity u_∞) at the actuator outlets and time-averaged streamlines near the outlets. The direction of normal and tangential component is illustrated in Figure 13 with the x-axis x_{sj}.

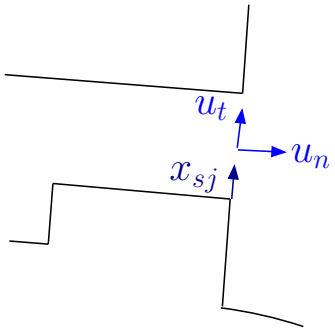

Figure 13: Coordinate system attached on the SS (top) actuator outlet. The coordinate system is flipped at the PS (bottom) actuator outlet, so that the point $x_{sj} = 0$ is close to the chord line. The direction of positive u_t is from the point $x_{sj} = 0$ to the outer edge of the actuator (or to the freestream).

ences between the simulation and experiments are observed, which appear to be features of the experimental configuration (the open slot in the side walls) that could not be represented in the computation.

Acknowledgments

This work is supported by United States Air Force Office of Scientific Research (AFOSR grant FA9550-05-10411).

REFERENCES

[1] Riou, J., Garnier, E., Deck, S., and Basdevant, C., "Improvement of Delayed-Detached Eddy Simulation Applied to Separated Flow Over Missile Fin," *AIAA Journal*, Vol. 47, No. 2, Feb. 2009, pp. 345–360.

[2] Deck, S., Duveau, P., d'Espiney, P., and Guillen, P., "Development and application of Spalart-Allmaras one equation turbulence model to three-dimensional supersonic complex configurations," *Aerospace Science and Technology*, Vol. 6, No. 3, May 2002, pp. 171–183.

[3] Brzozowski, D., Culp, J., and Glezer, A., "Active Control of Aerodynamic Forces on a Rapidly Maneuvering Airfoil," *Bulletin of the American Physical Society, Program of the 62nd Meeting of the Division of Fluid Dynamics*, 2009.

[4] DeSalvo, M. E. and Glezer, A., "Control of airfoil aerodynamics performance using distributed trapped vorticity," *AIAA-2007-0708*, 2007.

[5] Brzozowski, D. P., Culp, J. R., Kutay, A. T., Muse, J. A., and Glezer, A., "Closed-Loop Aerodynamic Flow Control of a Free Airfoil," *AIAA 2008-4323*, 2008.

[6] Greenblatt, D., Paschal, K. B., Yao, C. S., Harris, J., Schaeffler, N. N. W., and Washburn, A. E., "Experimental investigation of separation control - Part 1: Baseline and steady suction," *AIAA Journal*, Vol. 44, No. 12, 2006, pp. 2820–2830.

[7] Greenblatt, D. and Wygnanski, I. J., "The control of flow separation by periodic excitation," *Progress In Aerospace Sciences*, Vol. 36, No. 7, Oct. 2000, pp. 487–545.

[8] Muse, J. A., Kutay, A. T., Brozozowski, D. P., Culp, J. R., Calise, A. J., and Glezer, A., "Dynamic flight maneuvering using trapped vorticity flow control," *AIAA 2008-522*, 2008.

[9] Lopez, O. D., *Computational Study of a NACA4415 airfoil using synthetic jet control*, Ph.D. thesis, The University of Texas at Austin, 2009.

[10] Lopez, O., Brozozowski, D., Glezer, A., and Moser, R., "Aerodynamic Performance of Airfoils with Tangential Synthetic Jet Actuators Close to the Trailing Edge," *AIAA-2009-3674*, 2009.

[11] Jee, S. K., Lopez, O., Moser, R., Kutay, A., Muse, J., and Calise, A., "Flow Simulation of a Controlled Airfoil with Synthetic Jet Actuators," *AIAA-2009-3673*, 2009.

[12] Spalart, P. R. and Allmaras, S. R., "A one-equation turbulence model for aerodynamics flows," *La Recherche Aerospatiale*, Vol. 1, 1994, pp. 5–21.

[13] Spalart, P. R., Jou, W. H., Strelets, M., and Allmaras, S. R., "Comments on the feasibility of LES for wings and on a hybrid RANS/LES approach," *Proceedings of first AFOSR international conference on DNS/LES*, 1997.

[14] Spalart, P., Deck, S., Shur, M., Squires, K., Strelets, M., and Travin, A., "A new version of detached-eddy simulation, resistant to ambiguous grid densities," *Theoretical and Computational Fluid Dynamics*, Vol. 20, No. 3, JUL 2006, pp. 181–195.

[15] Ham, F. and Iaccarino, G., "Energy conservation in collocated discretization schemes on unstructured meshes," *Center of Turbulence Research Annual Research Briefs*, 2004, pp. 3–14.

[16] Abbott, I. H. and von Doenhoff, A. E., *Theory of Wing Sections*, Dover Publications, Inc., 1959.

[17] Hoffmann, M. J., Ramsay, R. R., and Gregorek, G. M., "Effects of Grit Roughness and Pitch Oscillations on the NACA 4415 Airfoil," Tech. rep., The Ohio State University, 1996.